



Grounding-line dynamics in a Stokes ice-flow model (Elmer/Ice v9.0): Improved numerical stability allows larger time steps

A. Clara J. Henry^{1,2}, Thomas Zwinger³, and Josefin Ahlkrona^{1,2,4}

Correspondence: A. Clara J. Henry (clara.henry@math.su.se)

Abstract.

10

The efficient and accurate simulation of grounding line dynamics in marine ice-sheet models remains a challenge, largely due to restrictive time-step limitations. The restrictive time step size of ice-sheet simulations ($\sim \Delta t = 0.01-0.5$ years) has led to the routine use of approximate models that compromise physical complexity compared to full Stokes models. To address the time-step restriction and enhance the applicability of full Stokes simulations, we implement a numerical stabilisation scheme at the ice-ocean interface, namely the Free-Surface Stabilisation Algorithm (FSSA). The FSSA acts by predicting the surface elevation at the next time step, resulting in a reduction in surface oscillations and an increase in the largest numerically stable time step. When applied to the ice-ocean interface, FSSA acts in combination with the *sea spring* numerical stabilisation scheme, allowing larger time steps to be taken.

In order to test the capabilities of the FSSA when applied to the ice-ocean interface, we perform the benchmark simulation of Experiment 3a from the Marine Ice Sheet Model Intercomparison Project (MISMIP). These simulations demonstrate the ability of the model to capture grounding line migration on both prograde slopes (oceanward sloping) and retrograde slopes (inland sloping). We find a time step size of $\Delta t = 10$ years to be numerically stable and accurate in the MISMIP experiment, which is more than an order of magnitude larger than the small time steps traditionally used. In comparison, a time-step size of $\Delta t = 50$ years can maintain numerical stability, but is not capable of capturing the full range of grounding-line motion in the MISMIP experiments. We further demonstrate the applicability of the FSSA to a 3D marine terminating model domain, finding that a time-step size of $\Delta t = 10$ years is numerically stable. The increase in the largest numerically stable time step by greater than an order of magnitude in marine-terminating Stokes ice-flow problems through the inclusion of FSSA broadens the applicability of Stokes models, which have otherwise been deemed too computationally expensive for large-scale applications.

20 1 Introduction

The Antarctic and Greenland Ice Sheets collectively hold an ice volume with a sea-level equivalent of 65.3 m (Morlighem et al., 2017, 2020). The loss of ice from these two remaining ice sheets has the potential to significantly influence global sea level, but projection uncertainties persist due to model variability (Fox-Kemper et al., 2021). The mass balance of the coastal regions of

¹Department of Mathematics, Stockholm University, Stockholm, Sweden

²Bolin Centre for Climate Research, Stockholm University, Stockholm, Sweden

³CSC-IT Center for Science, Espoo, Finland

⁴Swedish e-Science Research Centre, Stockholm, Sweden





ice sheets is particularly susceptible to changes in accumulation and melt (Donat-Magnin et al., 2021; Višnjević et al., 2025). Furthermore, these regions are characterised by complex flow dynamics at the grounding line, where the ice transitions from grounded to floating. The ability to accurately capture grounding-line dynamics in ice-sheet models is particularly important because a retreating or advancing grounding line induces a change in ice volume and influences the sea level. Furthermore, when the bed slopes inland, the grounding line can be subject to the marine ice-sheet instability (MISI), in which outlet glaciers undergo irreversible retreat and mass loss when the grounding line lies on a retrograde sloping bed (Weertman, 1974; Schoof, 2007; Favier et al., 2014; Joughin et al., 2014).

It has been recognised that the mesh resolution at the grounding line has an influence on its dynamic evolution in ice sheet models (Durand et al., 2009b; Williams et al., 2025). Many studies have implemented an adaptive mesh algorithm to allow simulations to be performed with a high resolution at the grounding line and a coarser resolution elsewhere (Durand et al., 2009b; Goldberg et al., 2009; Gladstone et al., 2010, 2012; Gagliardini et al., 2016; Dos Santos et al., 2019). However, such high resolutions are not feasible in continental-scale simulations, so alternative approaches have been developed. These include sub-grid methods (Cheng et al., 2020) or reduced-order modelling (Larour et al., 2012; Seroussi et al., 2014).

The modelling of ice flow in coastal regions is particularly challenging because high-complexity, high-resolution nonlinear Stokes models are needed for accuracy (Rückamp et al., 2022). Since such models require significant computational resources, lower-order approximate models are predominantly used for continental-scale simulations. Only a small number of ice-sheet codes support the use of a full nonlinear Stokes solver for ice-flow modelling (e.g. Elmer/Ice; Gagliardini et al. (2013)) and are regarded as benchmark models against which lower-order models are compared. However, widespread adoption of full Stokes models is hindered by their computational expense and is exacerbated by a restrictive time-step size stemming from numerical stability issues. Our work builds on many previous theoretical (Fowler, 1986; Schoof, 2005) and finite-element (Gagliardini et al., 2007; Stubblefield et al., 2021; de Diego et al., 2022) studies of contact problems in subglacial cavities and grounding-line Stokes problems. Other work also investigated the effect of the chosen friction law and grounding-line discretisation of the transition in boundary conditions (Gagliardini et al., 2016; Brondex et al., 2017, 2019). However, few studies have investigated improving the computational efficiency of full-Stokes contact problems (Durand et al., 2009a; Cheng et al., 2020).

In order to improve the numerical stability and applicability of Stokes simulations with an ice-ocean interface, we introduce the Free-Surface Stabilisation Algorithm (FSSA; Kaus et al. (2010); Löfgren et al. (2022); Löfgren et al. (2024)) at the ice-ocean interface. The FSSA mimics an implicit time-stepping scheme by predicting the free surface elevation in the next time step to account for an increase or decrease in ice thickness. The FSSA improves on the previously implemented *sea spring* numerical stabilisation scheme (Durand et al., 2009a).

To analyse the efficiency and accuracy of Stokes ice-flow simulations when including the FSSA, we perform simulations ranging from (1) a 2D marine ice-sheet domain set up with advancing and retreating phases of grounding line migration using the Marine Ice Sheet Model Intercomparison Project (MISMIP) framework (Pattyn et al., 2012), to (2) 3D simulations of Ekström Ice Shelf in Dronning Maud Land, East Antarctica. This study provides progress toward the routine use of full Stokes models in regions with complex stress regimes such as grounding-line dynamics by allowing an increase in computational efficiency due to a larger numerically-stable time step size.





2 Methods

In this section, we provide details of the ice-flow model, which is implemented in the finite element software Elmer/Ice (v9.0, Gagliardini et al., 2013; Ruokolainen et al., 2023).

2.1 Stokes model

Ice is a highly viscous, shear-thinning fluid, with conservation of momentum described by the Stokes equations,

$$\nabla \cdot \boldsymbol{\sigma} = \rho_{\mathbf{i}} \boldsymbol{g},\tag{1}$$

where σ is the Cauchy stress tensor, ρ_i is the ice density, and $\mathbf{g} = (0, 0, g)$ is the gravitational acceleration. The Cauchy stress tensor can be split into pressure, p, and a deviatoric stress tensor, τ ,

$$\sigma = \tau - pI, \tag{2}$$

where I is the identity matrix. The conservation of mass is expressed as an incompressibility condition,

$$\nabla \cdot \boldsymbol{u} = 0, \tag{3}$$

where $u = (u_x, u_y, u_z)$ is the velocity vector. In order to relate the nonlinear response of the strain rate of ice to an applied stress, Glen's flow law is used,

$$\tau = 2\eta(\dot{\boldsymbol{\varepsilon}})\dot{\boldsymbol{\varepsilon}},\tag{4}$$

where $\dot{\varepsilon}$ is the symmetric part of the velocity gradient tensor, i.e. $\dot{\varepsilon} = \frac{1}{2}(\nabla u + \nabla u^{\mathrm{T}})$. The effective viscosity, $\eta = \eta(\dot{\varepsilon})$, is defined as

75
$$\eta = \frac{1}{2}A^{-1/n} \left(\dot{\varepsilon}_{\text{crit}}^2 + \frac{1}{2} ||\dot{\varepsilon}||_F^2 \right)^{(1-n)/2n}$$
 (5)

Here, the effective strain-rate, $||\dot{\varepsilon}||_{\rm F}$, is the Frobenius norm of the strain rate tensor, which can be written $||\dot{\varepsilon}||_{\rm F} = \sqrt{{\rm tr}(\frac{1}{2}\dot{\varepsilon}^2)}$. The rheological parameter, A, controls the fluidity of the ice and is spatially constant in this study, but is temporally-varying in specified simulations (Section 4). A regularisation term, $\dot{\varepsilon}_{\rm crit}^2 = 10^{-15}~{\rm a}^{-1}$, is included to numerically stabilise the viscosity as the strain rate approaches zero.

0 2.2 Stokes boundary conditions

The Stokes equations are solved on a domain Ω , with a Cartesian coordinate system, $\mathbf{x} = (x, y, z) \in \mathbb{R}^3$. Boundary conditions are applied at the domain boundary $\partial\Omega$. The ice-atmosphere interface is denoted by Γ_a , the ice-bed interface by Γ_b , the ice-ocean interface by Γ_c , the calving front by Γ_c , and the ice divide by Γ_d so that $\partial\Omega = \Gamma_a \cup \Gamma_b \cup \Gamma_c \cup \Gamma_d$. During a transient





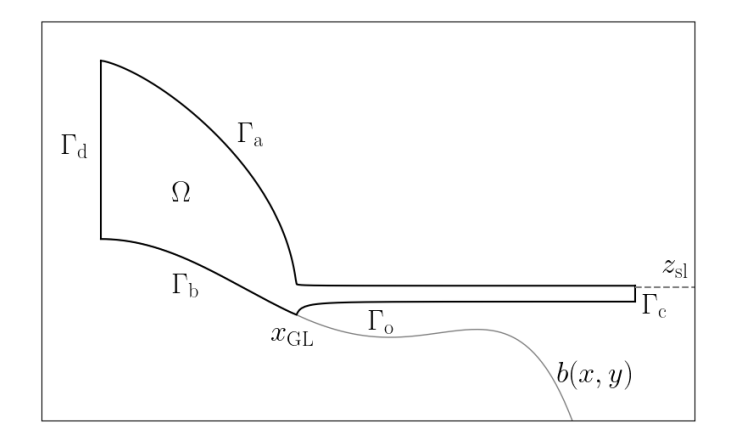


Figure 1. A schematic for the idealised 2D MISMIP Exp 3a set up. The model is also applied to a 3D, real-world ice sheet—ice shelf set up. The model domain, Ω , and the domain boundaries, $\partial\Omega = \Gamma_a \cup \Gamma_b \cup \Gamma_c \cup \Gamma_d$ are shown in 2D. The ice-atmosphere interface is denoted by Γ_a , the ice-bed interface by Γ_b , the ice-ocean interface by Γ_c , the calving front by Γ_c and the ice divide by Γ_d . The sea level is denoted by $z_{\rm sl}$, the grounding-line position by $z_{\rm sl}$ and the bed elevation by $z_{\rm sl}$.

simulation, the floating and grounded boundaries evolve to reflect changes in the grounding-line position. At the ice-atmosphere interface, Γ_a , a stress-free boundary condition is applied,

$$\boldsymbol{\sigma} \cdot \hat{\boldsymbol{n}} = 0, \tag{6}$$

where \hat{n} is the normal vector perpendicular to the ice surface and pointing outwards and is implicitly included in the weak form.

The ice-bed interface is subject to a Weertman-type friction law motivated by the set up in the Marine Ice Sheet Model Intercomparison Project (MISMIP, Pattyn et al. (2012)),

$$\boldsymbol{t}_i \cdot (\boldsymbol{\sigma} \cdot \hat{\boldsymbol{n}}) = -C|\boldsymbol{u}_b|^{m-1} \boldsymbol{u} \cdot \boldsymbol{t}_i, \tag{7}$$

where for each $i \in \{1,2\}$, t_i represents a vector tangential to the plane defined by the ice-bed interface. An impenetrability condition is applied to ice that is in contact with the bed,

$$\boldsymbol{u} \cdot \hat{\boldsymbol{n}} = 0. \tag{8}$$

At the boundaries, which are in contact with the ocean, Γ_{o} and Γ_{c} , the stress normal to the boundary is prescribed by the ocean pressure as,

$$\boldsymbol{\sigma} \cdot \hat{\boldsymbol{n}} = -p_{\mathbf{w}} \hat{\boldsymbol{n}},\tag{9}$$

where \hat{n} is the outward-pointing vector normal to the surface and the ocean pressure, $p_{\rm w}(z,t)$, is defined by

$$p_{\mathbf{w}}(z,t) = \begin{cases} \rho_{\mathbf{w}} g(z_{\mathrm{sl}}(t) - z) & \text{if } z < z_{\mathrm{sl}}(t), \\ 0 & \text{if } z \geq z_{\mathrm{sl}}(t), \end{cases}$$





where $\rho_{\rm w}$ is the ocean density and $z_{\rm sl}$ is the sea level. Where the ice-ocean interface, $\Gamma_{\rm o}$, and the ice-bed interface, $\Gamma_{\rm b}$, meet, the respective boundary conditions are discontinuous at the nodes representing the grounding line (Gagliardini et al., 2016). Finally, at the ice divide, $\Gamma_{\rm d}$, a symmetry condition is applied,

$$\boldsymbol{u} \cdot \hat{\boldsymbol{n}} = 0. \tag{10}$$

The Stokes equations are written in their weak form in order for the velocity and pressure to be solved using the finite element method with Elmer/Ice (Gagliardini et al., 2013). Multiplying by a test function, $v \in \mathbb{R}^3$, and integrating over the model domain, Ω , the weak form of the Stokes equations reads

$$\int_{\Omega} (\nabla \cdot \boldsymbol{\sigma}) \cdot \boldsymbol{v} \, d\Omega = \int_{\Omega} \boldsymbol{f} \cdot \boldsymbol{v} \, d\Omega. \tag{11}$$

On weak form, the incompressibility condition is written

$$-\int_{\Omega} (\nabla \cdot \boldsymbol{u}) q \, d\Omega = 0, \tag{12}$$

where $q \in \mathbb{R}$ is also a test function. Inserting the boundary conditions above results in the weak form of the Stokes equations applied to a marine-terminating ice sheet

$$-\int_{\Omega} \boldsymbol{\tau} : \nabla \boldsymbol{v} \, d\Omega - \int_{\Gamma_{o} \cup \Gamma_{c}} p_{w} \hat{\boldsymbol{n}} \cdot \boldsymbol{v} \, d\Gamma - \int_{\Gamma_{b}} C |\boldsymbol{u}_{b}|^{m-1} \boldsymbol{u}_{b} \cdot \boldsymbol{v} \, d\Gamma + \int_{\Omega} p \nabla \cdot \boldsymbol{v} \, d\Omega = \int_{\Omega} \boldsymbol{f} \cdot \boldsymbol{v} \, d\Omega.$$

$$(13)$$

The friction law is nonlinear, so it must be treated carefully when solved numerically. The nonlinear coefficient, $C|u_b|^{m-1}$, is evaluated at the previous iteration, j-1, for inclusion in the current iteration, j.

115 2.3 Free-surface evolution equations

The upper ice surface, $z = z_s(x, y, t)$, evolves subject to an evolution equation defined by,

$$\frac{\partial z_{\rm s}}{\partial t} + u_x \frac{\partial z_{\rm s}}{\partial x} + u_y \frac{\partial z_{\rm s}}{\partial y} = u_z + a_{\rm s},\tag{14}$$

where $a_s = a_s(x, y, t)$ is the surface accumulation rate. Similarly, the lower ice surface evolves subject to

$$\frac{\partial z_{\rm b}}{\partial t} + u_x \frac{\partial z_{\rm b}}{\partial x} + u_y \frac{\partial z_{\rm b}}{\partial y} = u_z + a_{\rm b},\tag{15}$$

where a_b is the basal melt (if $a_b > 0$) or accretion rate at the lower ice surface. The modelled ice is subject to constraints to ensure that the ice thickness does not become too thin. A constraint is placed on the upper ice surface so that

$$z_{\rm s}(x,y,t) - H_{\rm min} \ge z_{\rm b}(x,y,t),\tag{16}$$

The lower ice surface is subject to a constraint ensuring impenetrability,

$$z_{\mathbf{b}}(x,y,t) > b(x,y). \tag{17}$$





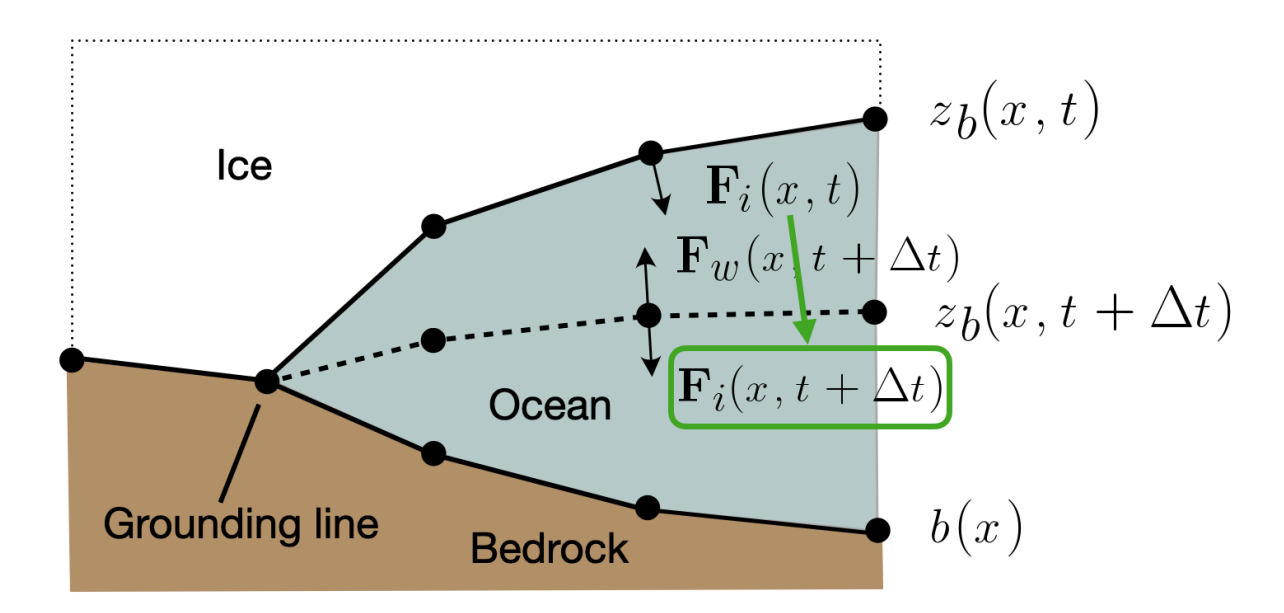


Figure 2. The balance of forces at the ice-ocean boundary. The force due to the ocean pressure, $F_{\rm w}(x,t+\Delta t)$, is evaluated at the next time step due to the *sea spring* numerical stabilisation scheme. Prior to this study, the ice load, $F_{\rm i}(x,t)$, was evaluated at the current time step. By introduction of the FSSA at the ice-ocean interface, the ice load is also evaluated at the next time step. The bed elevation is denoted by b(x), the lower ice surface elevation at the current time step is denoted by $z_{\rm b}(x,t)$. The predicted lower ice surface elevation at the next time step is denoted by $z_{\rm b}(x,t)$.

Here, b(x,y) is the bed elevation and H_{\min} is the minimum ice thickness. The elevation of the lower ice surface, $z_{\rm b}$, also depends on the dynamics of the grounding line, which is determined by the balance between the contact force and the water pressure.

During a transient simulation, the grounding line position must be allowed to migrate to reflect the altering ice geometry and velocity. Once a new grounding line position is determined, the application of boundary conditions must be altered accordingly. To determine whether to apply a friction law and an impenetrability condition or whether to apply ocean pressure and a free-slip condition at a particular node, the normal stress and the ocean pressure are examined through an algorithm presented in (Durand et al., 2009a).

3 Numerical stabilisation of free-surface Stokes problems

135

The coupling between the Stokes equations and the free-surface dynamics leads to a stiff system, in which the presence of fast-decaying modes (associated with large-magnitude eigenvalues) imposes a severe restriction on the maximum stable time step size, particularly for the explicit time integration methods traditionally used in ice sheet modelling (Löfgren et al., 2022). Solving the system of equations implicitly alleviates the need for a small time step. However, due to the elliptical nature of





the Stokes equations, the coupled system of the Stokes and the free-surface equations cannot be fully implicit in the velocity. Physically, this means that a deviation from hydrostatic equilibrium can produce large vertical velocities in the Stokes solution, which, when coupled to the upper and lower free surfaces equations, leads to an overshoot of the upper and lower ice surfaces. In turn, this causes oscillatory behaviour and numerical instability even for very small time steps. To reduce these time step size restrictions, two numerical stabilisation schemes are used here. Firstly, the standard *sea spring* numerical stabilisation scheme (Durand et al., 2009a) is used, which treats the ocean pressure term implicitly, and the Free-Surface Stabilisation Scheme (FSSA; Kaus et al. (2010)) is implemented, which treats the ice load implicitly. Thus far, the FSSA has shown promising results for grounded ice (Löfgren et al., 2022; Löfgren et al., 2024), but has not previously been implemented for grounding line and floating ice problems. Such model domains are particularly numerically challenging due to sharp gradients in the grounding zone and increased stiffness of the problem.

3.1 The sea spring numerical stabilisation scheme

To stabilise the contact problem, a numerical stabilisation scheme called *sea spring* was implemented on the lower ice surface in (Durand et al., 2009a). The *sea spring* numerical stabilisation scheme predicts the lower ice surface, z_b , in the next time step and adjusts the ocean pressure accordingly. The ocean pressure term before numerical stabilisation reads

$$\sigma_{\rm nn}|_{\rm b}(x,y,t) = -\rho_{\rm w}g(z_{\rm sl} - z_{\rm b}(x,y,t)) \tag{18}$$

and is evaluated on the current time step, t. Here, $z_{\rm sl}$ represents the sea level. The lower ice surface elevation at the next time step is predicted using an estimate of the vertical displacement, so that

55
$$z_{\rm b}(x,y,t+\Delta t) \approx z_{\rm b}(x,y,t) + (\boldsymbol{u}\cdot\hat{\boldsymbol{n}})\Delta t \sqrt{1 + \left(\frac{\partial z_{\rm b}(x,y,t)}{\partial x}\right)^2 + \left(\frac{\partial z_{\rm b}(x,y,t)}{\partial y}\right)^2},$$
 (19)

where Δt is the time step size and $t + \Delta t$ is the next time step. The ocean pressure term therefore becomes

$$\sigma_{\rm nn}|_{\rm b}(x,y,t) = -\rho_{\rm w}g \left\{ z_{\rm sl} - z_{\rm b}(x,y,t) + (\boldsymbol{u} \cdot \hat{\boldsymbol{n}})\Delta t \sqrt{1 + \left(\frac{\partial z_{\rm b}(x,y,t)}{\partial x}\right)^2 + \left(\frac{\partial z_{\rm b}(x,y,t)}{\partial y}\right)^2} \right\}$$
(20)

3.2 The Free-Surface Stabilisation Algorithm (FSSA)

The Free-Surface Stabilisation Algorithm (FSSA), was introduced by Kaus et al. (2010) to a Stokes problem with a free surface applied to mantle convection simulations. This method was later extended to Stokes free-surface problems in grounded ice-sheet modelling, proving successful in increasing the largest stable time step size (Löfgren et al., 2022; Löfgren et al., 2024). Here we will derive the FSSA for floating ice. The FSSA predicts the free-surface elevation at the next time step, $t + \Delta t$, and includes extra terms as boundary conditions to account for the adjustment in ice load. However, contrary to the expression for the ocean pressure, the free surface does not enter explicitly in the formulation for the ice load, but rather through the integral associated with the weak form. The FSSA is derived from the Reynold's Transport Theorem,

$$\frac{d}{dt} \int_{\Omega(t)} f \, d\Omega = \int_{\Omega(t)} \frac{\partial f}{\partial t} \, d\Omega + \int_{\partial \Omega(t)} (\boldsymbol{u} \cdot \hat{\boldsymbol{n}}) f \, d\Gamma, \tag{21}$$





where f is a physical quantity, $\Omega(t)$ is the model domain at time step t and $\partial\Omega(t)$ is the domain boundary at time step t. For our purposes, we take $f = -\rho_i \mathbf{g} \cdot \mathbf{v}$, i.e. the right hand side of the Stokes equations multiplied by the test function, \mathbf{v} . Assuming that f is time independent, and discretising in time, an approximation is found for the integral of f over the time-discretised domain, at the next time step, Ω^{k+1} , based on the current time step, k, so that

$$\int_{\Omega^{k+1}} f \, d\Omega \approx \int_{\Omega^k} f \, d\Omega + \Delta t \int_{\partial \Omega^k} (\boldsymbol{u} \cdot \hat{\boldsymbol{n}}) f \, d\Gamma. \tag{22}$$

The driving force term, i.e. the right hand side of the Stokes equations, therefore becomes

$$\int_{\Omega^{k+1}} \rho_{i} \boldsymbol{g} \cdot \boldsymbol{v} d\Omega \approx \int_{\Omega^{k}} \rho_{i} \boldsymbol{g} \cdot \boldsymbol{v} d\Omega + \Delta t \int_{\Gamma^{k}} (\boldsymbol{u} \cdot \hat{\boldsymbol{n}}) \rho_{i} \boldsymbol{g} \cdot \boldsymbol{v} d\Gamma + \Delta t \int_{\Gamma^{k}} (\boldsymbol{u} \cdot \hat{\boldsymbol{n}}) \rho_{i} \boldsymbol{g} \cdot \boldsymbol{v} d\Gamma,$$
(23)

where the last two terms represent the predicted upper and lower ice surfaces at the next time step, with an impenetrability condition, $u \cdot \hat{n} = 0$, at the ice divide and at the ice-bed interface. FSSA is not applied at the calving front because the mesh does not move horizontally here. If an accumulation and melt rate are to be included, two additional terms are added to represent the resulting vertical displacement,

$$\int_{\Omega^{k+1}} \rho_{i} \boldsymbol{g} \cdot \boldsymbol{v} d\Omega \approx \int_{\Omega^{k}} \rho_{i} \boldsymbol{g} \cdot \boldsymbol{v} d\Omega + \Delta t \int_{\Gamma_{a}^{k}} (\boldsymbol{u} \cdot \hat{\boldsymbol{n}}) \rho_{i} \boldsymbol{g} \cdot \boldsymbol{v} d\Gamma + \Delta t \int_{\Gamma_{o}^{k}} (\boldsymbol{u} \cdot \hat{\boldsymbol{n}}) \rho_{i} \boldsymbol{g} \cdot \boldsymbol{v} d\Gamma
+ \Delta t \int_{\Gamma_{a}^{k}} (a_{s} \hat{\boldsymbol{e}}_{z} \cdot \hat{\boldsymbol{n}}) (\boldsymbol{f} \cdot \boldsymbol{v}) d\Gamma + \Delta t \int_{\Gamma_{a}^{k}} (a_{b} \hat{\boldsymbol{e}}_{z} \cdot \hat{\boldsymbol{n}}) (\boldsymbol{f} \cdot \boldsymbol{v}) d\Gamma$$
(24)

The Stokes equations on weak form with the FSSA and the sea spring numerical stabilisation scheme therefore become

$$-\int_{\Omega^{k}} \boldsymbol{\tau} : \nabla \boldsymbol{v} d\Omega - \int_{\Gamma_{o}^{k} \cup \Gamma_{c,z<0}^{k}} \rho_{w} g \Delta t(\boldsymbol{u} \cdot \hat{\boldsymbol{n}}) \sqrt{1 + \left(\frac{\partial z_{b}}{\partial x}\right)^{2} + \left(\frac{\partial z_{b}}{\partial y}\right)^{2}} \hat{\boldsymbol{n}} \cdot \boldsymbol{v} d\Gamma$$

$$180 \quad -\int_{\Gamma_{b}^{k}} (C|\boldsymbol{u}_{b}|^{m-1} \boldsymbol{u}_{b} \cdot \boldsymbol{v} d\Gamma + \int_{\Omega^{k}} p \nabla \cdot \boldsymbol{v} d\Omega - \theta \Delta t \int_{\Gamma_{a}^{k}} (\boldsymbol{u} \cdot \hat{\boldsymbol{n}}) \rho_{i} \boldsymbol{g} \cdot \boldsymbol{v} d\Gamma - \theta \Delta t \int_{\Gamma_{o}^{k}} (\boldsymbol{u} \cdot \hat{\boldsymbol{n}}) \rho_{i} \boldsymbol{g} \cdot \boldsymbol{v} d\Gamma$$

$$= \int_{\Omega^{k}} \rho_{i} \boldsymbol{g} \cdot \boldsymbol{v} d\Omega - \int_{\Gamma_{o}^{k} \cup \Gamma_{c,z<0}^{k}} \rho_{w} g z_{b} d\Gamma + \theta \Delta t \int_{\Gamma_{a}^{k}} (a_{s} \hat{\boldsymbol{e}}_{z} \cdot \hat{\boldsymbol{n}}) (\boldsymbol{f} \cdot \boldsymbol{v}) d\Gamma + \theta \Delta t \int_{\Gamma_{o}^{k}} (a_{b} \hat{\boldsymbol{e}}_{z} \cdot \hat{\boldsymbol{n}}) (\boldsymbol{f} \cdot \boldsymbol{v}) d\Gamma$$

$$(25)$$

where we have assumed the sea level to be $z_{\rm sl}=0$ and the ocean pressure was applied only on the portion of the calving front in contact with the ocean, $\Gamma_{{\rm c},z<0}$. Since the calving front, $\Gamma_{\rm o}$, does not move horizontally, the FSSA terms are identical to zero there. Here, the parameter θ has been introduced to allow adjustment of the FSSA terms. A value of $\theta=0$ disables the FSSA terms, while a value of $\theta=1$ fully activates the FSSA terms. Finally, the weak form of the incompressibility condition reads

185
$$-\int_{\Omega^k} \nabla \cdot \tilde{\boldsymbol{u}}^{k+1} q \, d\Omega = 0. \tag{26}$$

Terms involving the solution variables, u and p are placed on the left hand side and the remaining terms are placed on the right hand side. During discretization and global assembly, the left hand side is split into the mass matrix, K, and the solution vector, U and the right hand side is the force vector, F.



200

205



Table 1. The model parameters implemented in Elmer/Ice for the 2D MISMIP Exp. 3a (Pattyn et al., 2012), used to investigate the application of the FSSA to the ice-ocean interface. The temporally-varying ice fluidity, *A*, is defined below in Table 2.

Parameter	Symbol	Value	Units
Gravity	g	-9.8	$m s^2$
Ice density	$ ho_{ m i}$	900	${\rm kg}{\rm m}^{-3}$
Water density	$ ho_{ m o}$	1000	${\rm kg}{\rm m}^{-3}$
Glen's exponent	n	3	
Surface mass balance	$a_{ m s}$	0.3	${\rm ma}^{-1}$
Friction coefficient	C	7.624×10^6	${ m Pa}{ m m}^{-1/3}{ m s}^{1/3}$
Friction exponent	m	1/3	

Note that whether the FSSA and *sea spring* are active or not at the lower and upper ice surfaces has an effect on the force balance at those surfaces due to the opposing ice load and ocean pressure. In the case of the *sea spring* numerical stabilisation, the ocean pressure is calculated at the predicted surface at the next time step. As a result, the ocean pressure contribution in the Stokes equations is higher in an advancing case, i.e. when the ice is thickening, compared to evaluating the ocean pressure at the current ice surface. The opposite is true in the retreating case, i.e. the ocean pressure contribution is lower with *sea spring* because it predicts thinner ice. In contrast, including the FSSA term at the lower ice surface predicts a higher ice load in an advancing case due to the prediction of thicker ice and a lower ice load in a retreating case due to the prediction of thinner ice.

4 Idealised numerical experiments - the MISMIP experiment

In order to investigate the speedup and accuracy of the FSSA across various spatial and temporal resolutions in simulations of marine ice sheets, we choose to perform experiments with the Marine Ice Sheet Model Intercomparison Project (MISMIP, Pattyn et al. (2012)) framework. The MISMIP experiments test the ability of models to capture the marine ice-sheet instability (MISI), whereby the position of the grounding line is stable on prograde slopes and unstable on retrograde slopes (Schoof, 2007; Durand et al., 2009a). The ability of models to capture MISI is paramount for accurately simulating past and future grounding-line migration and the associated sea-level contribution of glaciers such as Thwaites and Pine Island, which are particularly susceptible (Bett et al., 2024).

The focus of this part of the study is on the MISMIP Experiment 3a (Durand et al., 2009a; Pattyn et al., 2012). We use this setup to investigate the size of the largest stable time-step size as well as the accuracy when using FSSA. We also study the effect of the improved force balance in floating ice when including both the FSSA and the *sea spring* numerical stabilisation schemes and compare simulation runtimes.





Table 2. The ice fluidity, A, for the time intervals outlined in the MISMIP Exp. 3a (Pattyn et al., 2012). Note that the ice fluidity decreases in steps 1-7 and increases in steps 7-13.

Step	$A [s^{-1} Pa^{-3}]$	Time interval [a]
1	3×10^{-25}	3×10^4
2	2.5×10^{-25}	3×10^4
3	2×10^{-25}	3×10^4
4	1.5×10^{-25}	3×10^4
5	1×10^{-25}	3×10^4
6	5×10^{-26}	3×10^4
7	2.5×10^{-26}	3×10^4
8	5×10^{-26}	3×10^4
9	1×10^{-25}	3×10^4
10	1.5×10^{-25}	3×10^4
11	2×10^{-25}	3×10^4
12	2.5×10^{-25}	3×10^4
13	3×10^{-25}	3×10^4

4.1 Numerical experiments

Simulations with FSSA activated ($\theta=1$) are performed with time-step sizes of $\Delta t=0.5, 10$ and 50 years and varying grounding zone resolution (Table 3). A reference simulation of the full advance and retreat phases without the FSSA terms ($\theta=0$) is performed for a time step size of $\Delta t=0.5$ and a grounding-zone horizontal resolution of 200 m (Table 3). All simulations were subject to a small time step of 0.5 years for 1000 years after the ice fluidity jump in the retreating phase of Exp. 3a. When a small time step size was not used for a short period of time during the ice fluidity jump, the upper and lower surfaces, as well as the velocity field, exhibited oscillatory behaviour, leading to numerical stability.

215 The MISMIP Exp. 3a is defined by a 2D modelling domain of a marine ice sheet with the *x*-axis denoting the horizontal direction and the *z*-axis denoting the vertical direction. We apply the Stokes model and assume invariance in the *y*-direction. The bed elevation for Exp. 3a is defined as

$$b(x) = 729 - 2184.8 \left(\frac{x}{750000}\right)^2 + 1031.72 \left(\frac{x}{750000}\right)^4 - 151.72 \left(\frac{x}{750000}\right)^6.$$
 (27)

The model domain is initialised with a 10 m thick ice sheet and ice shelf. Initially, the floating ice is prescribed to be in hydrostatic equilibrium, a constraint which is only enforced to construct the initial geometry. The model parameters remain fixed throughout the simulations, with the exception of the ice fluidity A, and are defined in Table (1). The ice fluidity, A, is altered at 12 time points during the simulation, according to the values provided in Table (2). The step-wise change in fluidity induces grounding-line advance as the ice becomes stiffer (decreasing A) and grounding-line retreat as the ice becomes softer (increasing A). The experiment is carried out over a period of 285 000 years and demonstrates the typical hysteretic behaviour



230

235

240



Table 3. The choice of parameters for the simulations using the MISMIP Exp. 3a modelling framework. Only parameter choices yielding stable results are listed. The parameters are the time step size, Δt , the horizontal grounding-zone resolution, Δx , and the parameter controlling the activation of the FSSA, θ . This parameter takes the value $\theta = 1$ when the FSSA is active and $\theta = 1$ when the FSSA is inactive.

Δt [a]	Δx [m]	θ
0.5	200	0
0.5	200	1
10	25	1
10	50	1
10	100	1
10	200	1
50	25	1
50	50	1
50	100	1
50	200	1

of the grounding line in areas of alternating pro- and retrograde slopes. As outlined in the MISMIP study (Pattyn et al., 2012), the first 10 000 years of Exp. 3a are prone to numerical instability due to the thin, unrealistic nature of the domain. We chose a numerically-stable set up, which allowed quick simulation of these first 10 000 years. The chosen setup was performed with a time step size of $\Delta t = 10$ years and a horizontal resolution of $\Delta x = 2000$ m throughout the domain. Each simulation in our experiment, as outlined in Table 3, is performed beginning with the geometry at $t = 10\,000$ years.

Meshes are constructed from a 1D footprint mesh, which is vertically extruded to 20 layers, forming a terrain-following mesh consisting of quadrilateral elements. The footprint is refined in the areas either side of the grounding line position, in a 20 km wide area that we refer to as the grounding-zone hereafter. The grounding zone resolutions tested are $\Delta x = 25,50,100$ and 200 m (Table 3). Outside the refined area, a gradually decreasing horizontal resolution is applied to avoid large jumps in element size from the refined to the more coarsely resolved area, i.e. to ensure good mesh quality. Every 500 years, the mesh is updated, ensuring that the grounding line always remains within the area of refined horizontal resolution. The number of nodes in the area with a coarser horizontal resolution is defined in such a way that the number remains the same throughout the simulations. The simulations with a refined horizontal resolution of $\Delta x = 25$ m contain 98 679 nodes, those with $\Delta x = 50$ m contain $56\,679$ nodes, those with $\Delta x = 100$ m contain $35\,679$ nodes and those with $\Delta x = 200$ m contain $25\,179$ nodes. Each node has 3 degrees of freedom, corresponding to the horizontal velocities, (u_x, u_z) , and pressure, p.

Linear finite elements for velocity and pressure are used, with the Bubbles stabilisation (Baiocchi et al., 1993). The choice of linear elements is justified by the convergence tests in Gagliardini et al. (2013), which showed no improvement in accuracy when using quadratic elements for velocity and linear elements for pressure. The Stokes equations are solved using the Multifrontal Massively Parallel sparse direct Solver (MUMPS, (Amestoy et al., 2001)). In each time-step, first the Stokes equations are solved, followed by the upper free-surface and finally the lower free-surface equation.





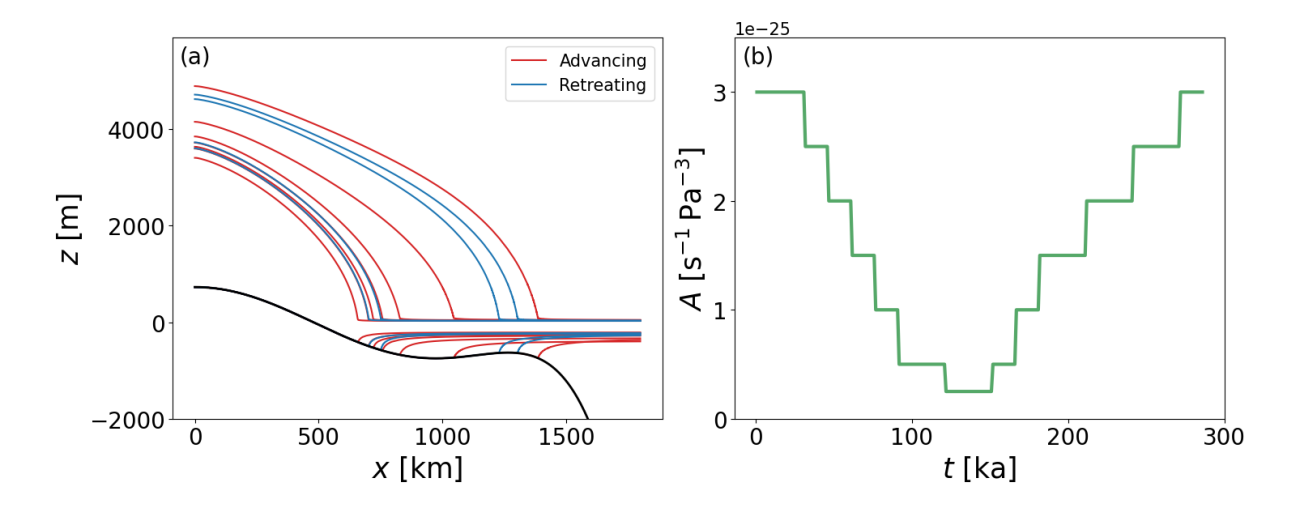


Figure 3. The MISMIP Exp. 3a (Pattyn et al., 2012) is designed to demonstrate grounding line migration over prograde and retrograde slopes, see the solid black line showing the bed elevation in (a). The movement of the grounding line is induced by altering the ice fluidity, A, at certain intervals during transient simulation as seen in (b). As the ice fluidity is reduced, the grounding line advances (red lines, (a)) and as the ice fluidity is increased, the grounding line retreats (blue lines, (a)).

Picard fixed point iterations are used to resolve the non-linear viscosity, with a nonlinear system convergence tolerance of 10^{-5} using a relaxation factor of 0.9. The free surface equations (14) and (15) are solved semi-implicitly, using a velocity from the last Stokes iteration (i.e explicit treatment) but an implicit treatment of the surface itself, using a backwards difference formula (BDF) time-stepping scheme of first order (i.e., implicit Euler). The linear convergence tolerance is set to 10^{-6} for both the upper and lower ice surfaces using the biconjugate gradient stabilised (BiCGStab) method, preconditioned using incomplete LU factorisation (ILU0). The minimum ice thickness is set to 10 m and is activated when solving the free-surface evolution equation for the upper ice surface. Due to the variational inequality, which sets the upper and lower limits of the free surfaces, nonlinear iterations with a convergence tolerance is set to 10^{-5} are performed to solve the free surface evolution equation. The streamline upwind/Petrov-Galerkin (SUPG) method is used for numerical stabilisation of the free surface solvers (Franca and Frey, 1992). These 2D simulations were performed in serial.

4.2 Results

255

260

The grounding line first advances and then retreats. Directly after each jump in ice fluidity, A, the grounding line advanced or retreated more rapidly for a period of time before slowing down. The slope of the bed also had an influence on how rapidly the grounding line advanced or retreated. During advance, the grounding line was first on a prograde slope. Once it had advanced enough to reach the area with a retrograde slope, it advanced more rapidly. In the retreating phase, the grounding line retreated more rapidly when on the retrograde slope and more slowly on the prograde slope.





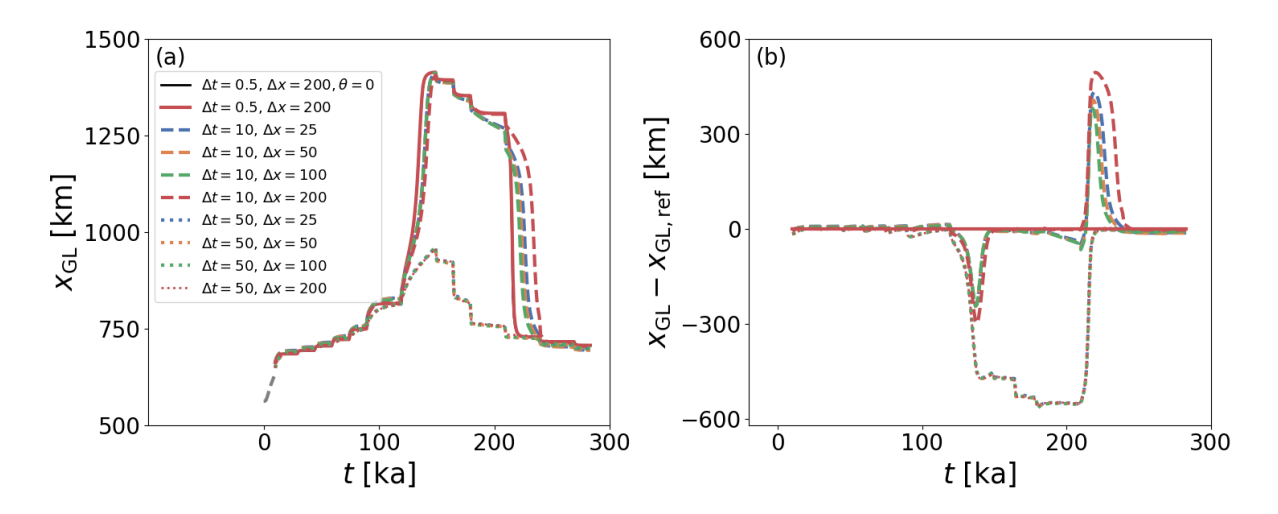


Figure 4. (a) The grounding line position, $x_{\rm GL}$, is plotted against the simulation time, t. (b) The difference between the grounding line position, $x_{\rm GL}$, of each simulation compared with the reference grounding line position, $x_{\rm GL,ref}$. The solid lines indicate a time step size of $\Delta t = 0.5$ years, the dashed lines indicate a time step size of $\Delta t = 10$ years and the dotted lines indicate a time step size of $\Delta t = 50$ years. The line colours indicate the horizontal resolution in the refined area encompassing the grounding line. Blue indicates a resolution of $\Delta x = 25$ m, orange a resolution of $\Delta x = 50$ m, green a resolution of $\Delta x = 100$ m, and red a resolution of $\Delta x = 200$ m.

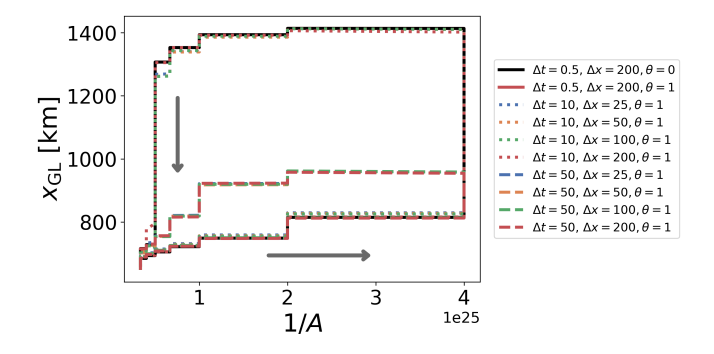


Figure 5. The hysteretic behaviour of the grounding line on alternating retro- and prograde slopes according to the MISMIP Exp. 3a. The grounding line position, $x_{\rm GL}$ is plotted as a function of the inverse ice fluidity, 1/A, across various time step sizes and grounding-zone horizontal resolutions. All simulations are stabilised with the FSSA ($\theta = 1$) except for the simulation with a set up of $\Delta t = 0.5$, $\Delta x = 200, \theta = 0$.



270

275

280

285

290



Even for small time-step sizes, much lower than those presented here, no simulation was possible without sea spring. Simulations without the FSSA ($\theta=0$) were not numerically stable with time step sizes of 10 and 50 years. The FSSA-stabilised simulations with a time-step size of $\Delta t=10$ and $\Delta t=50$ years were numerically stable. The simulations with $\Delta t=10$ also showed high accuracy (Fig. 4.2). With this time-step size, the maximum grounding line extent ranged from 1413 km in the case of the simulation with a horizontal grounding-zone resolution of $\Delta x=25$ m to 1406 km in the case of the simulation with a horizontal grounding-zone resolution of $\Delta x=200$ m, both close to the maximum grounding line extent of 1414 km in the reference simulation with $\Delta t=0.5$, $\Delta x=200$ and $\theta=0$.

The simulations with $\Delta t=10$ lagged behind the reference simulations during rapid grounding line advance, i.e. when the grounding line position was on the retrograde slope and the grounding line position was unstable. The maximum lag of the grounding line position ranged from of 244 km in the case of the simulation with $\Delta x=25\,\mathrm{m}$ to $297\,\mathrm{m}$ with a horizontal grounding-zone resolution of $\Delta x=200\,\mathrm{m}$. During rapid grounding line retreat, when the grounding line position was unstable, the simulations lagged further behind the reference simulation, with the $\Delta x=25\,\mathrm{simulation}$ lagging a maximum of $431\,\mathrm{km}$ and the $\Delta x=200\,\mathrm{simulation}$ lagging a maximum of $494\,\mathrm{km}$ behind the reference simulation. There is no clear relation between spatial resolution and the lag. This lag occurs despite the precaution of applying a small time step size of $0.5\,\mathrm{years}$ immediately after each ice fluidity jump.

In the simulations with a time-step size of $\Delta t = 50$ years, the grounding line did not follow the full hysteretic behaviour expected of this experiment, although approximately the same steady state was eventually reached, and the simulation was very accurate in phases of slow migration. The grounding line reached maximum extents ranging between 958 and 962 km (depending on the resolution $\Delta x = 25, 50, 100$, and 200 m) compared with a maximum extent of 1414 km in the reference simulation.

In Fig. 4.2 there is no significant difference between simulations with and without FSSA for a small time-step size of $\Delta t=0.5$ when analysed on the timescale of the entire MISMIP experiment. However, during periods of rapid advance and retreat, a small difference is observed due to evaluating the ice load and the ocean pressure at the same time step ($\theta=1$) compared to at different time steps ($\theta=0$), see Fig. 4.2. There is a small influence on the grounding line position, with the simulation including the FSSA terms resulting in a grounding-line position on average 635 m further oceanward than the simulation without the FSSA. This trend of the simulation with FSSA having a grounding line further oceanward occurs throughout the simulations, with the simulation that includes the FSSA being on average 1030 m further oceanward in the advancing phase and 635 m further oceanward in the retreating phase. In other words, the grounding line advances more quickly and retreats more slowly in the simulation with the FSSA active ($\theta=1$) compared to the simulation without the FSSA terms ($\theta=0$).

Incorporating FSSA resulted in a significant improvement in computational efficiency compared to simulations without it (Fig. 4.2). Without the FSSA, a time step size of $\Delta t=2$ was possible, but a time step size of $\Delta t=5$ did not converge. In contrast, a time step size as large as 250 years is numerically stable using FSSA, albeit with error. The time step size of $\Delta t=50$ resulted in a speedup range of 38-43 compared to a time-step of 2, when measured from $t=10\,000$ for 500 years and the time





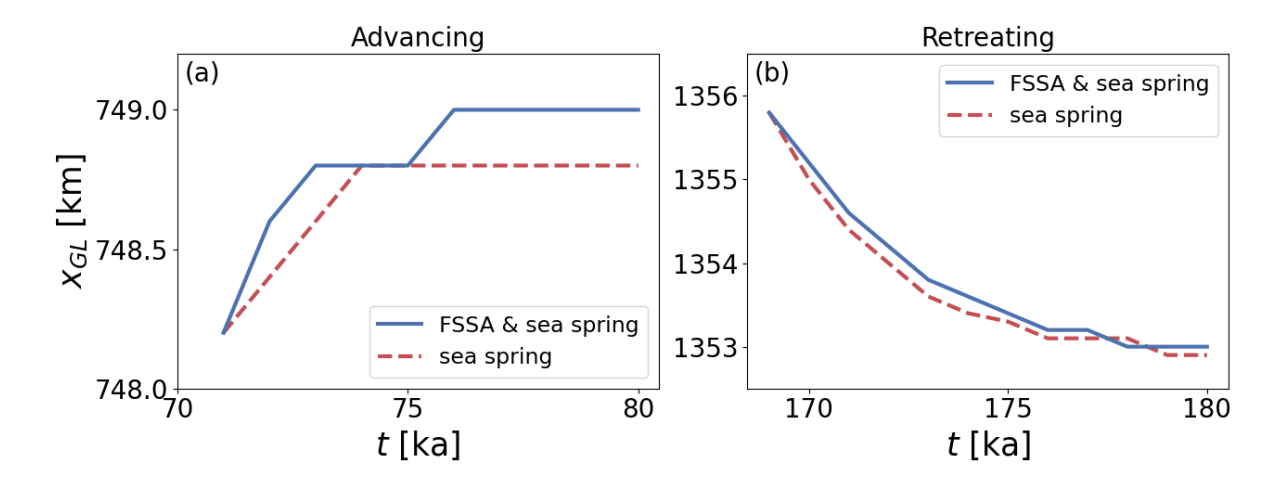


Figure 6. Grounding line migration in (a) during advance of the grounding line, and (b) during retreat of the grounding line. The blue curves indicate simulations which include both the *sea spring* numerical stabilisation scheme and the FSSA($\theta = 1$), while the dashed red curves indicate simulations with only the *sea spring* numerical stabilisation scheme ($\theta = 0$). These simulations have been performed with a refined mesh of 200 m in the area surrounding the grounding line and a time step size of 0.5 years.

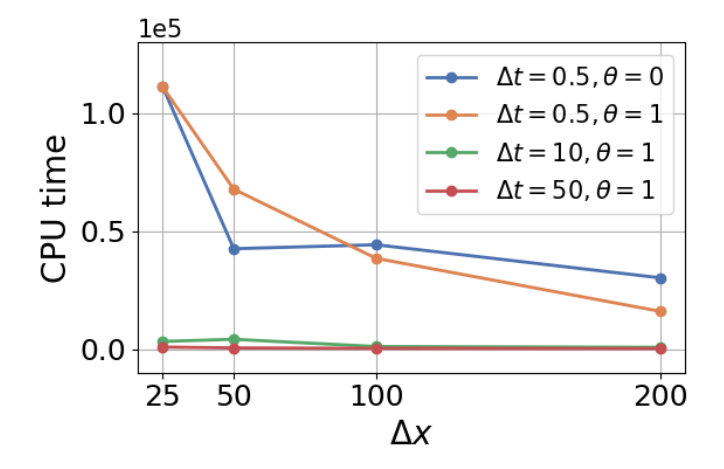


Figure 7. The CPU time for MISMIP Exp. 3a for 500 simulation years starting at $t = 10\,000$ year. The colours indicate the time step size, Δt , and whether the FSSA is active ($\theta = 1$) or inactive ($\theta = 0$). Results are shown for refined horizontal mesh resolutions of 25, 50, 100, and 200 m.



300

305

310

315

320



step size of $\Delta t = 10$ resulted in a speedup of 11. Comparing between horizontal grounding-zone resolutions of $\Delta x = 25$ m and the $\Delta x = 200$ m simulations with time step sizes of $\Delta t = 10$ and $\Delta t = 50$ were 4.4 and 3.8 times faster, respectively.

5 Application to Ekström Ice Shelf

5.1 Numerical experiments

In order to evaluate our FSSA modelling framework in the context of a 3D, real-world, grounding-line problem, we apply the FSSA-stabilised model to the Ekström Ice Shelf embayment in Dronning Maud Land, East Antarctica (Fig. 5.1). Ekström Ice Shelf has a length of ~ 120 km compared to a width of only ~ 50 km and is strongly influenced by lateral buttressing caused by the Søråsen and Halvfarryggen Ice Rises, resulting in a relatively thick ice shelf. Ekström Ice Shelf has been the subject of numerous studies, including comprehensive mapping of the ice shelf cavity and related studies (e.g. Neckel et al. (2012); Schannwell et al. (2019); Smith et al. (2020); Eisermann et al. (2020); Oetting et al. (2022)). Moving to a 3D, real-world setting allows validation of the FSSA across a variety of flow regimes and grounding line behaviours.

In order to model Ekström Ice Shelf, a number of changes were made in comparison to the idealised experiments above. Several parameters are given more accurate values (e.g. Morlighem et al. (2020)), as laid out in Table 4. The isothermal ice fluidity, A, and the friction coefficient, C, were tuned to values that caused minimal deviation from observed surface velocities (Rignot and Scheuchl., 2017). The geometry of the initial upper ice surface, the lower ice surface and the bed elevation were derived from Morlighem et al. (2020). For the surface accumulation rate, a_s , we used the results of the Regional Atmospheric Climate Model (RACMO2.3p1, (van den Broeke, 2019)). The basal melt rates are derived from Adusumilli et al. (2020) and a condition is applied to ensure that the melt occurs only at floating nodes. The surface accumulation rate and the basal melt rate are included in the free-surface evolution equations (Eqs. (14) and (15)), and the FSSA accumulation terms, i.e. the last two terms of Eq. (25). No smoothing of the initial upper and lower ice surface, the bed elevation nor the surface accumulation rate was made. However, significant fluctuations in the basal mass balance caused excess thinning of the ice in isolated areas and numerical instabilities regardless of whether the FSSA was active or not. Therefore, anomalies $> 4 \, \mathrm{m} \, \mathrm{a}^{-1}$ were removed and smoothing of the basal melt rate dataset was performed with a Gaussian filter.

The horizontal boundaries of the model domain were chosen along divides and streamlines, and close to the calving front. In the interior portion of the embayment, the low ice thickness ($< 10 \,\mathrm{m}$ in some areas) and the roughness of the bed caused numerical instability. We therefore chose to reduce the inland extent of the domain slightly to avoid these numerical instabilities, which is justified because the velocities are low in this area and have only a negligible influence on the overall ice-flow dynamics of the downstream embayment. Furthermore, the impenetrability condition of Eq. (10) is replaced with a normal Neumann velocity boundary condition with a coefficient chosen such that through-flow is negligible. This boundary condition takes the form

$$325 \quad \hat{\boldsymbol{n}} \cdot (\boldsymbol{\sigma} \cdot \hat{\boldsymbol{n}}) = -C_{n} \boldsymbol{u} \cdot \hat{\boldsymbol{n}}. \tag{28}$$





Table 4. The model parameters for the 3D Ekström ice shelf experiments to test the time step size and accuracy of transient simulations when applying the FSSA to the ice-ocean interface. All other model parameters are as in Table 1.

Parameter	Symbol	Value	Units
Ice density	$ ho_{ m i}$	917	${\rm kgm}^{-3}$
Water density	$ ho_{ m o}$	1028	${\rm kgm}^{-3}$
Ice fluidity	A	1.0×10^{-25}	${ m Pa}{ m m}^{-1/3}{ m s}^{1/3}$
Friction coefficient	C	1.0×10^{7}	$Pa m^{-1/3} s^{1/3}$

This formulation alleviated spurious artifacts at the ice divide, which occurred when implementing an impenetrability condition.

The 3D finite element mesh is constructed using an unstructured mesh footprint with a horizontal resolution of $\Delta x = 500$ m in an area 3000 m either side of the grounding line and a horizontal resolution of $\Delta x = 2000$ m elsewhere. The horizontal mesh footprint is vertically extruded for a total of 6 layers, allowing for high horizontal resolution at the grounding line and a reasonable compute time. The mesh contains 18343 nodes, meaning that there are 73372 degrees of freedom and the simulations are performed with 100 partitions. All other details described in Section 2 hold for the simulations of Ekström Ice Shelf.

Simulations varying in time-step size are performed of the Ekström Ice Shelf embayment to investigate the applicability of the FSSA to 3D, real-world, marine-terminating ice-sheet simulations. The time-step sizes chosen are $\Delta t = 0.5, 5, 10$ and 20, which were performed with $(\theta = 1)$ and without $(\theta = 0)$ the FSSA. The solver set up for the Stokes and free-surface solvers is the same as in the MISMIP experiments. Each simulation is performed for a period of 100 years after which the results are compared. In each time step, the Stokes solver is executed first, followed by the upper and lower free-surface solvers. The convergence tolerance for the nonlinear Stokes iterations is set to 10^{-5} . The convergence tolerances for the free surfaces also take the value 10^{-5} .

5.2 Results

330

335

340

345

350

Our analysis concentrates on a vertical cross-section, A-A', of the 3D model domain, which captures the grounded area, grounding zone and floating ice shelf (Figs. 5.1 and 5.1). Along this cross-section, the simulated ice thickness reaches a minimum of 519 m and a maximum of 870 m in the grounded ice. In contrast, the minimum and maximum ice thickness in the ice shelf along this cross-section are 178 m and 823 m. The grounded ice has a mean thickness of 724 m and the floating ice has a mean thickness of 483 m along this cross-section. This contrasts with the MISMIP Exp. 3a simulations, where lateral buttressing does not play a role due to the 2D model domain. Along the cross-section, the basal melt rate, $a_{\rm b}$, has significantly higher values than the surface accumulation rate, $a_{\rm s}$, with values reaching $1.9\,{\rm m\,a^{-1}}$ compared to $0.4\,{\rm m\,a^{-1}}$, respectively.

The three simulations which include the FSSA with time step sizes of $\Delta t = 0.5$, 5 and 10 years show good convergence and result in geometries which are very similar. The FSSA simulation ($\theta = 1$) with a time step size of $\Delta t = 20$ years does



355



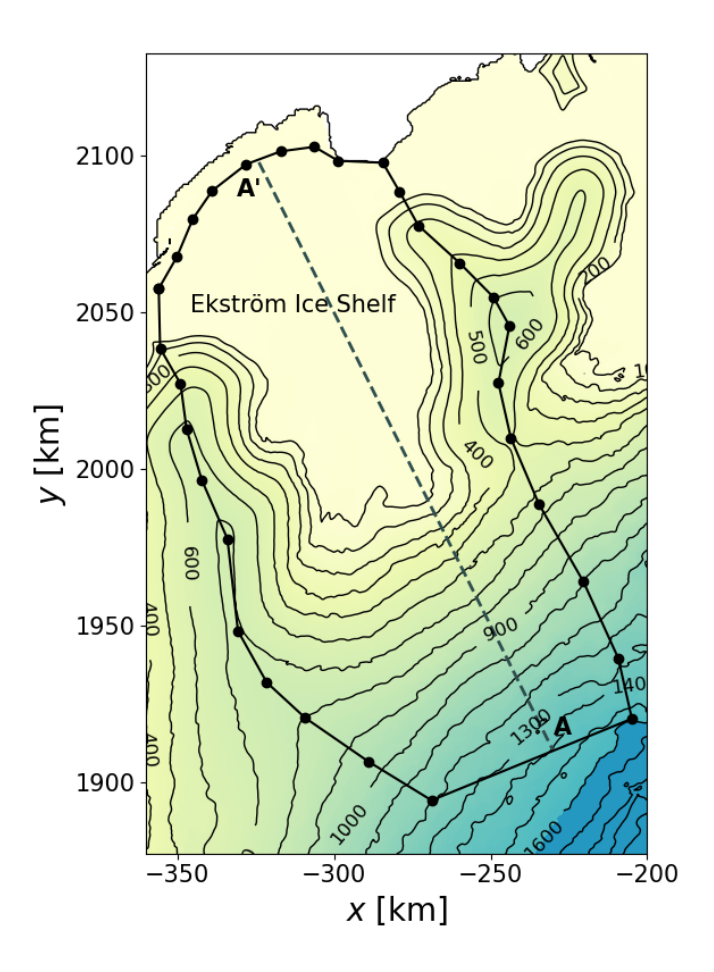


Figure 8. The upper ice surface elevation, z_s , relative to the mean sea level of Ekström Ice Shelf Embayment in Dronning Maud Land, East Antarctica. The solid line shows the model domain for the 3D full Stokes simulations of the embayment. The grey dashed line shows the location of a cross-section, A - A', made through the 3D simulation. The open ocean can be seen in white in the upper left corner.

not converge within 100 nonlinear iterations of the Stokes solver, even in the first time step. In contrast, the only simulation without the FSSA ($\theta=0$) to converge adequately throughout the simulation of 100 years is the simulation with a time step size of $\Delta t=0.5$. In the simulation with a time step size of $\Delta t=5$ and without the FSSA ($\theta=0$), the Stokes solver and the free surface solvers converge for the first 7 time steps before numerical instability occurs. In the simulations with the FSSA activated and time-step sizes of 0.5, 5, and 10, the maximum horizontal velocities reach magnitudes of 196, 105, and 74 m a⁻¹.

The simulations with a time step size of $\Delta t = 0.5$, with and without FSSA, show very little difference in Central Processing Unit (CPU) runtime when run over 100 simulation years, with just a 0.6% difference. However, when increasing the time step size to $\Delta t = 5$ or $\Delta t = 10$, the runtimes are 12% and 7% of the runtime of the $\Delta t = 0.5$ with FSSA inactive ($\theta = 0$).





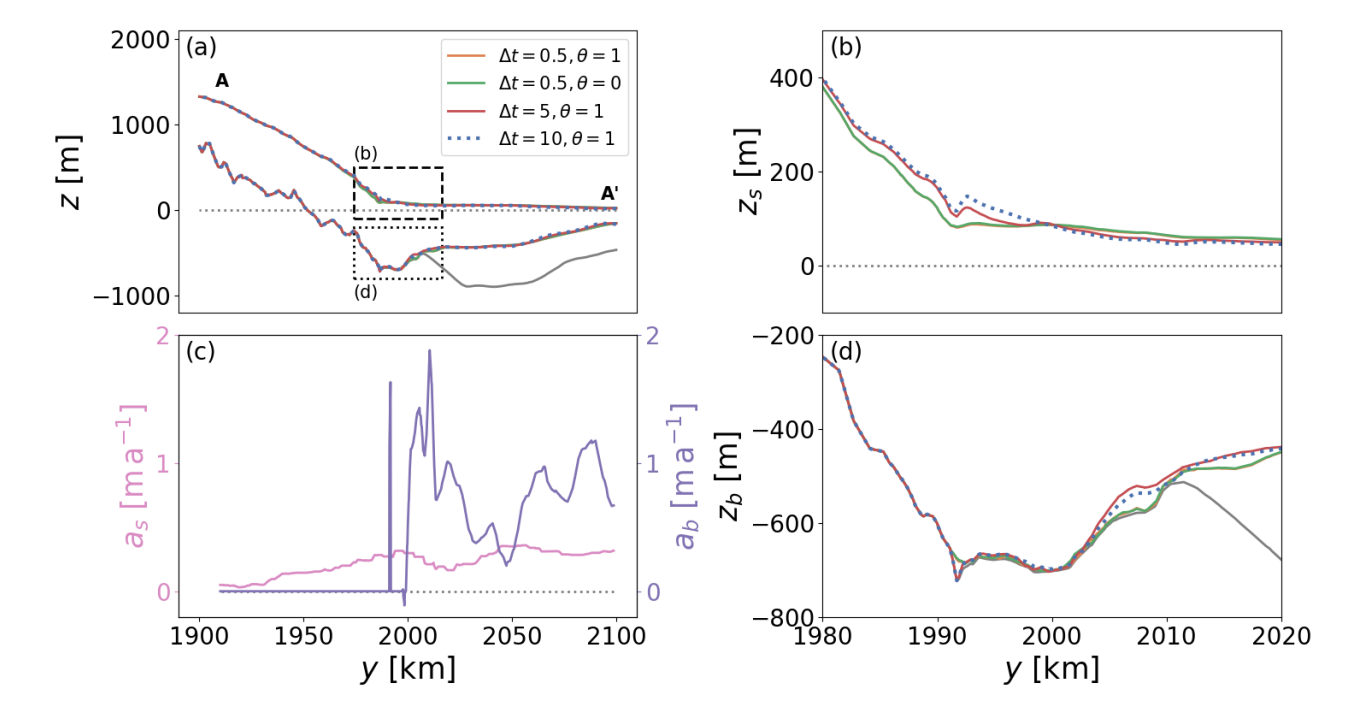


Figure 9. (a) A vertical cross-section of numerical simulations of the Ekström Ice Shelf embayment after transient evolution for 100 years. The location of the cross-section, A - A', is indicated in Fig. (5.1). The bed elevation is shown in grey and the sea level is shown as a black dotted line. Simulations of various time step sizes, Δt , and grounding-line horizontal mesh resolutions, Δx , are shown. (c) The surface accumulation rate, a_s (pink), and the basal melt rate, a_b (purple), are shown along the same cross-section as (a). The surface accumulation rate uses RACMO2.3p1, van den Broeke (2019)). A dataset from Adusumilli et al. (2020) is used for the basal melt rates. (b) & (d) The upper ice surface, z_s , and the lower ice surface, z_s , in the grounding-zone as indicated by dashed and dotted boxes in (a), respectively. (c) The lower ice surface, z_b , in the grounding-zone as indicated by the box with a dotted line in (a). The grey dotted line in (b) indicates the sea level and the grey solid line in (d) indicates the bed elevation.

6 Discussion

360

365

6.1 Efficient modelling of grounding-line dynamics

The findings of this study demonstrate that inclusion of the Free-Surface Stabilisation Algorithm (FSSA) at the ice-ocean interface significantly increases the largest numerically stable time step size of marine ice sheet simulations. In an idealised, 2D model setup, our results show that a time-step size of $\Delta = 50$ years is generally numerically stable but only accurate in phases of slow grounding line advance and retreat and that a time step size of $\Delta t = 10$ years provides high accuracy throughout most of the simulations. This indicates that the dynamical changes of grounding line problems does not require the small time-steps traditionally used, and that the requirement of such small time-steps is rather due to suboptimal numerical methods with poor stability properties. However, high time-step sizes require a small time step immediately after a viscosity



370

375

380

385



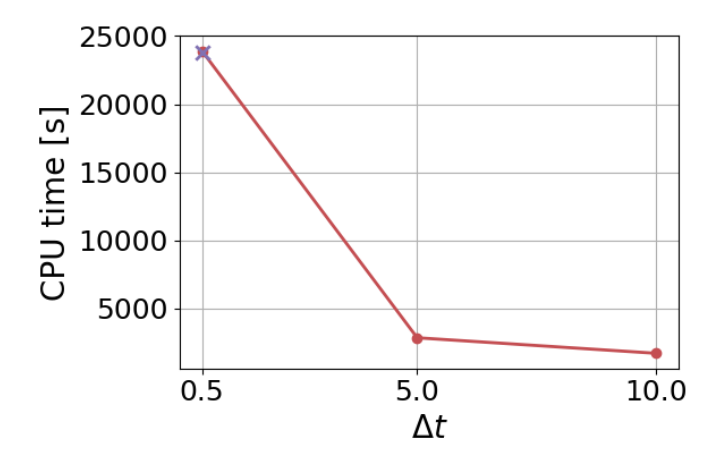


Figure 10. The CPU time for the Ekström Ice Shelf numerical simulations, performed with 100 simulation years starting at t = 0. The colours indicate whether the FSSA is active (red) or inactive (purple). Results are shown for time step sizes of 0.5, 5, and 10 years.

jump during the grounding-line retreat phase. In 100-year, 3D simulations of an embayment, a time step size of 10 years is found to be numerically stable and accurate when including the FSSA. We expect that an even higher time step size may be numerically stable after allowing further relaxation of the simulation, or correction of datasets which are prone to inaccuracy in the grounding zones (Morlighem et al., 2020). In light of our results, we recommend the use of an adaptive time-stepping scheme when incorporating the FSSA into Stokes simulations, with a large time step size being used when little change in the velocity and geometry occurs and a small time step size when significant change in the system occurs to ensure accuracy.

The FSSA accomplishes a significant speedup in CPU runtime by predicting where the ice surface will be in the next time step, thereby mimicking an implicit time-stepping scheme when calculating the velocities using the Stokes solver. This allows anticipation and dampening of large changes in the solution, therefore allowing larger time steps to be taken. Furthermore, this work builds on an additional numerical stabilisation scheme applied to the ice-ocean interface, namely the *sea spring* numerical stabilisation scheme (Durand et al., 2009a). The *sea spring* numerical stabilisation scheme is paramount to the stability of such marine ice sheet simulations, with a time step size much lower than those used here not converging without it. The inclusion of both numerical stabilisation schemes results in the ice load and the ocean pressure being evaluated at the next time step, ensuring that a mismatch in forces at the ice-ocean interface no longer occurs. This is evident in Fig. 4.2, where in both the advancing and retreating phases, the simulation with the FSSA terms is further oceanward. We hypothesis that this difference during the grounding-line advance is because the simulation with the FSSA terms predicts thicker ice and therefore a higher flux, which results in faster grounding-line advance, which is in line with the theory of Schoof (2007). In the retreating case, the opposite holds. The simulation with the FSSA terms predicts thinner ice and therefore a lower ice flux and slower grounding line retreat.



390

395

400

405

410



6.2 Implications for ice-sheet modelling

The FSSA is an easy-to-implement approach to improve numerical stability. Since the Stokes model captures the underlying physics more accurately than simplified models, this approach leads to improved overall precision in the results. The inclusion of FSSA in Stokes models of coastal regions, as demonstrated in our study, brings higher-order models closer to broad applicability. Unlike current large-scale ice-sheet models, full Stokes models do not assume hydrostatic equilibrium at the grounding line and include all stress components, allowing accurate simulation of grounding zones where the stress regimes switch from vertical-shearing dominated dynamics to horizontal stretching. While small time steps are needed for physical reasons such as rapid grounding line migration or short-term temporal variation in surface accumulation and melt rates, the speedup has significant potential during time frames when the ice geometry and velocity are close to equilibrium, in palaeo ice-sheet simulations or in spin-up simulations (Seroussi et al., 2019).

Further possibilities for a broader application of full Stokes models with the inclusion of FSSA include coupling frameworks with lower-order models (Ahlkrona et al., 2016; van Dongen et al., 2018; Seroussi et al., 2012). While FSSA enables greater numerical stability in physically complex areas such as grounding-zones, a coupling framework to a lower order model in areas where flow is less complicated will further improve model efficiency. The increased efficiency that FSSA offers has the potential to improve the applicability of simulations of ice stratigraphy, where high resolution and accurate ice flow physics are important (Henry et al., 2025; Bingham et al., 2024). Additionally, the improved efficiency has the potential for full Stokes models to be used in machine learning methods where a significant number of simulations need to be performed (Moss et al., 2025). Integrating the modelling framework with FSSA and an adaptive time-stepping scheme (Cheng et al., 2017) will allow the automated increase in efficiency while maintaining accuracy, particularly during rapid change such as grounding-line migration. While the FSSA mimicks an implicit time-stepping scheme, a fully implicit scheme would offer additional model accuracy and efficiency (Kramer et al., 2012; Bueler, 2024).

A number of problem-specific challenges remain, including the treatment of the minimum thickness constraint in combination with the FSSA, which posed a problem in initial simulations of the Ekström Ice Shelf embayment. In addition, further analysis of the discretisation schemes for application of friction and ocean pressure boundary conditions needs to be made, particularly by comparison with real-world geometries (Gagliardini et al., 2016). Further work is needed to extend well-posedness analysis and error estimation in relation to the time-dependent grounding-line contact problem (John et al., 2018; Helanow and Ahlkrona, 2018; de Diego et al., 2022). The applicability of full Stokes ice-sheet simulations will need to be tested beyond the geometries and model set up presented in this study.

415 7 Conclusions

In this study, we applied the Free-Surface Stabilisation Algorithm (FSSA) to the ice-ocean interface in 2D, idealised simulations and 3D, real-world simulations with the goal of improving the efficiency and applicability of complex, full Stokes models. Using the MISMIP Experiment 3a model setup (Pattyn et al., 2012), we simulated the advance and retreat of the grounding line on bed topography that transitions between pro- and retrograde slopes, capturing the characteristic hysteresis of such

https://doi.org/10.5194/egusphere-2025-4192 Preprint. Discussion started: 12 November 2025

© Author(s) 2025. CC BY 4.0 License.



440



geometries. Including the FSSA terms on both the upper and lower ice surfaces enabled a numerically stable time step size of $\Delta t = 50$ years, while a time step size of $\Delta t = 10$ resolved the benchmark hysteretic behaviour of the MISMIP Exp. 3a. To demonstrate the broader applicability of the 3D, marine-terminating Stokes simulations with the FSSA, we performed simulations of the Ekström Ice Shelf embayment in Dronning Maud Land, East Antarctica. Here, we found that a time step

size of $\Delta t = 10$ is numerically stable and produces minimal error in geometry.

The ability to solve a coupled Stokes flow and free-surface evolution problem with time steps significantly larger than typical time step sizes of $\sim \Delta t = 0.01-0.5$ years used in ice-sheet modelling offers an alternative to simplified models which often rely on assumptions such as a hydrostatic grounding line. Combining the FSSA with an adaptive time-stepping scheme (Cheng et al., 2017) has the potential to offer improved flexibility, particularly in simulations where fine-scale dynamics or the temporal resolution of assimilated data require small time steps. The inclusion of FSSA in Stokes marine ice-sheet simulations broadens

430 their applicability to large-scale domains, allowing an alternative to lower-order models, which neglect key physical details.

Code availability. The code used to run the simulations and the post-processing is published in a repository (https://doi.org/10.5281/zenodo.16909574, Henry, 2025a). The Elmer version is 9.0 (https://doi.org/10.5281/zenodo.7892181, Ruokolainen et al., 2023).

Data availability. The model output data are published in a repository (https://doi.org/10.5281/zenodo.16909985, Henry, 2025b).

Author contributions. ACJH set up the model and performed the simulations with support from TZ and JA, ACJH and JA conceptualised the study, ACJH performed the formal analysis, ACJH created the figures, ACJH wrote the original draft, which was edited by all authors.

Competing interests. The authors declare that there are no conflicts of interest.

Acknowledgements. ACJH is supported by the Wallenberg Foundation (KAW 2021.0275). JA was funded by the Swedish Research Council, grant number 2021-04001, as well as the Swedish e-Science Research Centre (SeRC). The contribution by Thomas Zwinger was supported by TerraDT - Digital Twin of Earth system for Cryosphere, Land surface and related interactions that has received funding from the European Union's Horizon Europe Framework Programme (HORIZON) under Grant Agreement no.101187992. The simulations were performed using resources provided by the PDC Center for High Performance Computing, Sweden. The authors acknowledge minimal assistance from ChatGPT (versions 4 & 5, OpenAI) for code development.





References

450

455

460

- Adusumilli, S., Fricker, H. A., Medley, B., Padman, L., and Siegfried, M. R.: Interannual variations in meltwater input to the Southern Ocean from Antarctic ice shelves, Nature geoscience, 13, 616–620, https://doi.org/10.1038/s41561-020-0616-z, 2020.
 - Ahlkrona, J., Lötstedt, P., Kirchner, N., and Zwinger, T.: Dynamically coupling the non-linear Stokes equations with the shallow ice approximation in glaciology: Description and first applications of the ISCAL method, Journal of Computational Physics, 308, 1–19, https://doi.org/10.1016/j.jcp.2015.12.025, 2016.
 - Amestoy, P., Duff, I. S., Koster, J., and L'Excellent, J.-Y.: A fully asynchronous multifrontal solver using distributed dynamic scheduling, SIAM Journal on Matrix Analysis and Applications, 23, 15–41, https://doi.org/10.1137/S0895479899358194, 2001.
 - Baiocchi, C., Brezzi, F., and Franca, L. P.: Virtual bubbles and Galerkin-least-squares type methods (Ga.L.S.), Computer Methods in Applied Mechanics and Engineering, 105, 125–141, https://doi.org/10.1016/0045-7825(93)90119-I, 1993.
 - Bett, D. T., Bradley, A. T., Williams, C. R., Holland, P. R., Arthern, R. J., and Goldberg, D. N.: Coupled ice-ocean interactions during future retreat of West Antarctic ice streams in the Amundsen Sea sector, The Cryosphere, 18, 2653–2675, https://doi.org/10.5194/tc-18-2653-2024, 2024.
 - Bingham, R. G., Bodart, J. A., Cavitte, M. G., Chung, A., Sanderson, R. J., Sutter, J. C., Eisen, O., Karlsson, N. B., MacGregor, J. A., Ross, N., et al.: Antarctica's internal architecture: Towards a radiostratigraphically-informed age-depth model of the Antarctic ice sheets, EGUsphere, 2024, 1–66, https://doi.org/10.5194/egusphere-2024-2593, 2024.
 - Brondex, J., Gagliardini, O., Gillet-Chaulet, F., and Durand, G.: Sensitivity of grounding line dynamics to the choice of the friction law, Journal of Glaciology, 63, 854–866, https://doi.org/10.1017/jog.2017.51, 2017.
 - Brondex, J., Gillet-Chaulet, F., and Gagliardini, O.: Sensitivity of centennial mass loss projections of the Amundsen basin to the friction law, The Cryosphere, 13, 177–195, https://doi.org/10.5194/tc-13-177-2019, 2019.
 - Bueler, E.: Surface elevation errors in finite element Stokes models for glacier evolution, arXiv preprint arXiv:2408.06470, 2024.
- Cheng, G., Lötstedt, P., and von Sydow, L.: Accurate and stable time stepping in ice sheet modeling, Journal of Computational Physics, 329, 465 29–47, https://doi.org/10.1016/j.jcp.2016.10.060, 2017.
 - Cheng, G., Lötstedt, P., and von Sydow, L.: A full Stokes subgrid scheme in two dimensions for simulation of grounding line migration in ice sheets using Elmer/ICE (v8. 3), Geoscientific Model Development, 13, 2245–2258, https://doi.org/10.5194/gmd-13-2245-2020, 2020.
 - de Diego, G. G., Farrell, P. E., and Hewitt, I. J.: Numerical approximation of viscous contact problems applied to glacial sliding, Journal of Fluid Mechanics, 938, A21, https://doi.org/10.1017/jfm.2022.178, 2022.
- Donat-Magnin, M., Jourdain, N. C., Kittel, C., Agosta, C., Amory, C., Gallée, H., Krinner, G., and Chekki, M.: Future surface mass balance and surface melt in the Amundsen sector of the West Antarctic Ice Sheet, The Cryosphere, 15, 571–593, https://doi.org/10.5194/tc-15-571-2021, 2021.
 - Dos Santos, T. D., Morlighem, M., Seroussi, H., Devloo, P. R. B., and Simões, J. C.: Implementation and performance of adaptive mesh refinement in the Ice Sheet System Model (ISSM v4. 14), Geoscientific Model Development, 12, 215–232, https://doi.org/10.5194/gmd-12-215-2019, 2019.
 - Durand, G., Gagliardini, O., de Fleurian, B., Zwinger, T., and Le Meur, E.: Marine ice sheet dynamics: Hysteresis and neutral equilibrium, Journal of Geophysical Research, 114, F03 009, https://doi.org/10.1029/2008JF001170, 2009a.
 - Durand, G., Gagliardini, O., Zwinger, T., Le Meur, E., and Hindmarsh, R. C.: Full Stokes modeling of marine ice sheets: influence of the grid size, Annals of Glaciology, 50, 109–114, https://doi.org/10.3189/172756409789624283, 2009b.



485

495



- Eisermann, H., Eagles, G., Ruppel, A., Smith, E. C., and Jokat, W.: Bathymetry beneath ice shelves of Western Dronning Maud Land, East Antarctica, and implications on ice shelf stability, Geophysical Research Letters, 47, e2019GL086724, https://doi.org/https://doi.org/10.1029/2019GL086724, e2019GL086724 2019GL086724, 2020.
 - Favier, L., Durand, G., Cornford, S. L., Gudmundsson, G. H., Gagliardini, O., Gillet-Chaulet, F., Zwinger, T., Payne, A., and Le Brocq, A. M.: Retreat of Pine Island Glacier controlled by marine ice-sheet instability, Nature Climate Change, 4, 117–121, https://doi.org/10.1038/nclimate2094, 2014.
 - Fowler, A.: A sliding law for glaciers of constant viscosity in the presence of subglacial cavitation, Proceedings of the Royal Society of London. A. Mathematical and Physical Sciences, 407, 147–170, https://doi.org/10.1098/rspa.1986.0090, 1986.
- Fox-Kemper, B., Hewitt, H., Xiao, C., Aðalgeirsdóttir, G., Drijfhout, S., Edwards, T., Golledge, N., Hemer, M., Kopp, R., Krinner, G., Mix, A., Notz, D., Nowicki, S., Nurhati, I., Ruiz, L., Sallée, J.-B., Slangen, A., and Yu, Y.: Ocean, Cryosphere and Sea Level Change., In Climate Change 2021: The Physical Science Basis. Contribution of Working Group I to the Sixth Assessment Report of the Intergovernmental Panel on Climate Change [MassonDelmotte, V., P. Zhai, A. Pirani, S.L. Connors, C. Péan, S. Berger, N. Caud, Y. Chen, L. Goldfarb, M.I. Gomis, M. Huang, K. Leitzell, E. Lonnoy, J.B.R. Matthews, T.K. Maycock, T. Waterfield, O. Yelekçi, R. Yu, and B. Zhou (eds.)]. Cambridge University Press. In Press., 2021.
 - Franca, L. P. and Frey, S. L.: Stabilized finite element methods: II. The incompressible Navier-Stokes equations, Computer Methods in Applied Mechanics and Engineering, 99, 209–233, https://doi.org/10.1016/0045-7825(92)90041-H, 1992.
 - Gagliardini, O., Cohen, D., Råback, P., and Zwinger, T.: Finite-element modeling of subglacial cavities and related friction law, Journal of Geophysical Research, 112, F02 027, https://doi.org/10.1029/2006JF000576, 2007.
 - Gagliardini, O., Zwinger, T., Gillet-Chaulet, F., Durand, G., Favier, L., de Fleurian, B., Greve, R., Malinen, M., Martín, C., Råback, P., Ruokolainen, J., Sacchettini, M., Schäfer, M., Seddik, H., and Thies, J.: Capabilities and performance of Elmer/Ice, a new-generation ice sheet model, Geoscientific Model Development, 6, 1299–1318, https://doi.org/10.5194/gmd-6-1299-2013, 2013.
 - Gagliardini, O., Brondex, J., Gillet-Chaulet, F., Tavard, L., Peyaud, V., and Durand, G.: Brief communication: Impact of mesh resolution for MISMIP and MISMIP3d experiments using Elmer/Ice, The Cryosphere, 10, 307–312, https://doi.org/10.5194/tc-10-307-2016, 2016.
 - Gladstone, R., Lee, V., Vieli, A., and Payne, A.: Grounding line migration in an adaptive mesh ice sheet model, Journal of Geophysical Research: Earth Surface, 115, https://doi.org/10.1029/2009JF001615, 2010.
- Gladstone, R. M., Payne, A. J., and Cornford, S. L.: Resolution requirements for grounding-line modelling: sensitivity to basal drag and ice-shelf buttressing, Annals of Glaciology, 53, 97–105, https://doi.org/10.3189/2012AoG60A148, 2012.
 - Goldberg, D., Holland, D. M., and Schoof, C.: Grounding line movement and ice shelf buttressing in marine ice sheets, Journal of Geophysical Research, 114, F04 026, https://doi.org/10.1029/2008JF001227, 2009.
- Helanow, C. and Ahlkrona, J.: Stabilized equal low-order finite elements in ice sheet modeling accuracy and robustness, Computational Geosciences, 22, 951–974, https://doi.org/10.1007/s10596-017-9713-5, 2018.
 - Henry, A., Schannwell, C., Višnjević, V., Millstein, J., Bons, P., Eisen, O., and Drews, R.: Predicting the three-dimensional stratigraphy of an ice rise, Journal of Geophysical Research: Earth Surface, 130, e2024JF007924, https://doi.org/10.1029/2024JF007924, 2025.
 - Henry, A. C. J.: A Fully Implicit Second Order Method for Viscous Free Surface Stokes Flow Application to Glacier Simulations" by Josefin Ahlkrona, André Löfgren and A. Clara J. Henry, https://doi.org/10.5281/zenodo.16909574, 2025a.
- Henry, A. C. J.: Model output data for the publication "Grounding- line dynamics in a Stokes ice-flow model: Improved numerical stability allows larger time steps", https://doi.org/10.5281/zenodo.16909985, 2025b.



530



- John, V., Knobloch, P., and Novo, J.: Finite elements for scalar convection-dominated equations and incompressible flow problems: a never ending story?, Computing and Visualization in Science, 19, 47–63, https://doi.org/10.1007/s00791-018-0290-5, 2018.
- Joughin, I., Smith, B. E., and Medley, B.: Marine ice sheet collapse potentially under way for the Thwaites Glacier Basin, West Antarctica, Science, 344, 735–738, https://doi.org/10.1126/science.1249055, 2014.
 - Kaus, B. J., Mühlhaus, H., and May, D. A.: A stabilization algorithm for geodynamic numerical simulations with a free surface, Physics of the Earth and Planetary Interiors, 181, 12–20, https://doi.org/10.1016/j.pepi.2010.04.007, 2010.
 - Kramer, S. C., Wilson, C. R., and Davies, D. R.: An implicit free surface algorithm for geodynamical simulations, Physics of the Earth and Planetary Interiors, 194, 25–37, https://doi.org/10.1016/j.pepi.2012.01.001, 2012.
- Larour, E., Seroussi, H., Morlighem, M., and Rignot, E.: Continental scale, high order, high spatial resolution, ice sheet modeling using the Ice Sheet System Model (ISSM), Journal of Geophysical Research: Earth Surface, 117, https://doi.org/https://doi.org/10.1029/2011JF002140, 2012.
 - Löfgren, A., Zwinger, T., Råback, P., Helanow, C., and Ahlkrona, J.: Increasing numerical stability of mountain valley glacier simulations: implementation and testing of free-surface stabilization in Elmer/Ice, The Cryosphere, 18, 3453–3470, https://doi.org/10.5194/tc-18-3453-2024, 2024.
 - Löfgren, A., Ahlkrona, J., and Helanow, C.: Increasing stable time-step sizes of the free-surface problem arising in ice-sheet simulations, Journal of Computational Physics: X, 16, 100114, https://doi.org/10.1016/j.jcpx.2022.100114, 2022.
 - Morlighem, M., Williams, C. N., Rignot, E., An, L., Arndt, J. E., Bamber, J. L., Catania, G., Chauché, N., Dowdeswell, J. A., Dorschel, B., et al.: BedMachine v3: Complete bed topography and ocean bathymetry mapping of Greenland from multibeam echo sounding combined with mass conservation, Geophysical Research Letters, 44, 11–051, https://doi.org/10.1002/2017GL074954, 2017.
 - Morlighem, M., Rignot, E., Binder, T., Blankenship, D., Drews, R., Eagles, G., Eisen, O., Ferraccioli, F., Forsberg, R., Fretwell, P., et al.: Deep glacial troughs and stabilizing ridges unveiled beneath the margins of the Antarctic ice sheet, Nature Geoscience, 13, 132–137, https://doi.org/10.1038/s41561-019-0510-8, 2020.
- Moss, G., Višnjević, V., Eisen, O., Oraschewski, F. M., Schröder, C., Macke, J. H., and Drews, R.: Simulation-based inference of surface accumulation and basal melt rates of an Antarctic ice shelf from isochronal layers, Journal of Glaciology, 71, e44, https://doi.org/10.1017/jog.2025.13, 2025.
 - Neckel, N., Drews, R., Rack, W., and Steinhage, D.: Basal melting at the Ekström Ice Shelf, Antarctica, estimated from mass flux divergence, Annals of Glaciology, 53, 294–302, https://doi.org/10.3189/2012AoG60A167, 2012.
- Oetting, A., Smith, E. C., Arndt, J. E., Dorschel, B., Drews, R., Ehlers, T. A., Gaedicke, C., Hofstede, C., Klages, J. P., Kuhn, G., Lambrecht,

 A., Läufer, A., Mayer, C., Tiedemann, R., Wilhelms, F., and Eisen, O.: Geomorphology and shallow sub-sea-floor structures underneath the Ekström Ice Shelf, Antarctica, The Cryosphere, 16, 2051–2066, https://doi.org/10.5194/tc-16-2051-2022, 2022.
 - Pattyn, F., Schoof, C., Perichon, L., Hindmarsh, R. C. A., Bueler, E., de Fleurian, B., Durand, G., Gagliardini, O., Gladstone, R., Goldberg, D., Gudmundsson, G. H., Huybrechts, P., Lee, V., Nick, F. M., Payne, A. J., Pollard, D., Rybak, O., Saito, F., and Vieli, A.: Results of the Marine Ice Sheet Model Intercomparison Project, MISMIP, The Cryosphere, 6, 573–588, https://doi.org/10.5194/tc-6-573-2012, 2012.
- 550 Rignot, E., J. M. and Scheuchl., B.: MEaSUREs InSAR-based Antarctica ice velocity map, Version 2, https://doi.org/10.5067/D7GK8F5J8M8R, 2017.
 - Rückamp, M., Kleiner, T., and Humbert, A.: Comparison of ice dynamics using full-Stokes and Blatter–Pattyn approximation: application to the Northeast Greenland Ice Stream, The Cryosphere, 16, 1675–1696, https://doi.org/10.5194/tc-16-1675-2022, 2022.



560

575



- Ruokolainen, J., Malinen, M., Råback, P., Zwinger, T., Takala, E., Kataja, J., Gillet-Chaulet, F., Ilvonen, S., Gladstone, R., Byckling, M.,

 Chekki, M., Gong, C., Ponomarev, P., van Dongen, E., Robertsen, F., Wheel, I., Cook, S., t7saeki, luzpaz, and Rich_B: ElmerCSC/elmerfem: Elmer 9.0, https://doi.org/10.5281/zenodo.7892181, 2023.
 - Schannwell, C., Drews, R., Ehlers, T. A., Eisen, O., Mayer, C., and Gillet-Chaulet, F.: Kinematic response of ice-rise divides to changes in ocean and atmosphere forcing, The Cryosphere, 13, 2673–2691, https://doi.org/10.5194/tc-13-2673-2019, 2019.
 - Schoof, C.: The effect of cavitation on glacier sliding, Proceedings of the Royal Society A: Mathematical, Physical and Engineering Sciences, 461, 609–627, https://doi.org/10.1098/rspa.2004.1350, 2005.
 - Schoof, C.: Ice sheet grounding line dynamics: Steady states, stability, and hysteresis, Journal of Geophysical Research, 112, F03S28, https://doi.org/10.1029/2006JF000664, 2007.
 - Seroussi, H., Ben Dhia, H., Morlighem, M., Larour, E., Rignot, E., and Aubry, D.: Coupling ice flow models of varying orders of complexity with the Tiling method, Journal of Glaciology, 58, 776–786, https://doi.org/10.3189/2012JoG11J195, 2012.
- Seroussi, H., Morlighem, M., Larour, E., Rignot, E., and Khazendar, A.: Hydrostatic grounding line parameterization in ice sheet models, The Cryosphere, 8, 2075–2087, https://doi.org/10.5194/tc-8-2075-2014, 2014.
 - Seroussi, H., Nowicki, S., Simon, E., Abe-Ouchi, A., Albrecht, T., Brondex, J., Cornford, S., Dumas, C., Gillet-Chaulet, F., Goelzer, H., Golledge, N. R., Gregory, J. M., Greve, R., Hoffman, M. J., Humbert, A., Huybrechts, P., Kleiner, T., Larour, E., Leguy, G., Lipscomb, W. H., Lowry, D., Mengel, M., Morlighem, M., Pattyn, F., Payne, A. J., Pollard, D., Price, S. F., Quiquet, A., Reerink, T. J., Reese, R.,
- Rodehacke, C. B., Schlegel, N.-J., Shepherd, A., Sun, S., Sutter, J., Van Breedam, J., van de Wal, R. S. W., Winkelmann, R., and Zhang, T.: initMIP-Antarctica: an ice sheet model initialization experiment of ISMIP6, The Cryosphere, 13, 1441–1471, https://doi.org/10.5194/tc-13-1441-2019, 2019.
 - Smith, E. C., Hattermann, T., Kuhn, G., Gaedicke, C., Berger, S., Drews, R., Ehlers, T. A., Franke, D., Gromig, R., Hofstede, C., et al.: Detailed seismic bathymetry beneath Ekström Ice Shelf, Antarctica: Implications for glacial history and ice-ocean interaction, Geophysical Research Letters, 47, e2019GL086187, https://doi.org/10.1029/2019GL086187, 2020.
 - Stubblefield, A. G., Spiegelman, M., and Creyts, T. T.: Variational formulation of marine ice-sheet and subglacial-lake grounding-line dynamics, Journal of Fluid Mechanics, 919, A23, https://doi.org/10.1017/jfm.2021.394, 2021.
 - van den Broeke, M. R.: RACMO2.3p1 annual surface mass balance Antarctica (1979-2014), https://doi.org/10.1594/PANGAEA.896940, 2019.
- van Dongen, E. C., Kirchner, N., Van Gijzen, M. B., Van de Wal, R. S., Zwinger, T., Cheng, G., Lötstedt, P., and Von Sydow, L.: Dynamically coupling full Stokes and shallow shelf approximation for marine ice sheet flow using Elmer/Ice (v8. 3), Geoscientific Model Development, 11, 4563–4576, https://doi.org/10.5194/gmd-11-4563-2018, 2018.
 - Višnjević, V., Moss, G., Henry, A. C. J., Wild, C. T., Steinhage, D., and Drews, R.: Mapping the composition of Antarctic ice shelves as a metric for their susceptibility to future climate change, Geophysical Research Letters, 52, e2024GL112585, https://doi.org/10.1029/2024GL112585, 2025.
 - Weertman, J.: Stability of the junction of an ice sheet and an ice shelf, Journal of Glaciology, 13, 3–11, https://doi.org/10.1017/S0022143000023327, 1974.
- Williams, C. R., Thodoroff, P., Arthern, R. J., Byrne, J., Hosking, J. S., Kaiser, M., Lawrence, N. D., and Kazlauskaite, I.: Calculations of extreme sea level rise scenarios are strongly dependent on ice sheet model resolution, Communications Earth & Environment, 6, 60, https://doi.org/10.1038/s43247-025-02010-z, 2025.